JACS
JOURNAL OF THE AMERICAN CHEMICAL SOCIETY
Article
pubs.acs.org/JACS

Conduction and Reactivity in Heterogeneous-Molecular Catalysis: New Insights in Water Oxidation Catalysis by Phosphate Cobalt Oxide Films

Cyrille Costentin,* Thomas R. Porter, and Jean-Michel Savéant*

Université Paris Diderot, Sorbonne Paris Cité, Laboratoire d'Electrochimie Moléculaire, Unité Mixte de Recherche Université−CNRS No. 7591, Bâtiment Lavoisier, 15 rue Jean de Baïf, 75205 Paris Cedex 13, France

Supporting Information

ABSTRACT: Cyclic voltammetry of phosphate cobalt oxide (CoP_i) films catalyzing O_2-evolution from water oxidation as a function of scan rate, phosphate concentration and film thickness allowed for new insights into the coupling between charge transport and catalysis. At pH = 7 and low buffer concentrations, the film is insulating below 0.8 (V vs SHE) but becomes conductive above 0.9 (V vs SHE). Between 1.0 to 1.3 (V vs SHE), the mesoporous structure of the film gives rise to a large thickness-dependent capacitance. At higher buffer concentrations, two reversible proton-coupled redox couples appear over the capacitive response with 0.94 and 1.19 (V vs SHE) pH = 7 standard potentials. The latter is, at most, very weakly catalytic and not responsible for the large catalytic current observed at higher potentials. CV-response analysis showed that the amount of redox-active cobalt-species in the film is small, less than 10% of total. The catalytic process involves a further proton-coupled-electron-transfer and is so fast that it is controlled by diffusion of phosphate, the catalyst cofactor. CV-analysis with newly derived relationships led to a combination of the catalyst standard potential with the catalytic rate constant and a lower-limit estimation of these parameters. The large currents resulting from the fast catalytic reaction result in significant potential losses related to charge transport through the film. CoP_i films appear to combine molecular catalysis with semiconductor-type charge transport. This mode of heterogeneous molecular catalysis is likely to occur in many other catalytic films.

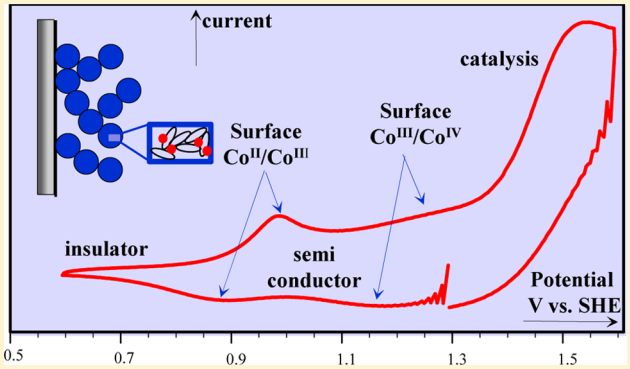

INTRODUCTION

Electrocatalytic water oxidation to generate molecular oxygen is a primary challenge in storing electrical energy in chemical bonds. This half reaction makes up one part of water splitting reaction used to generate molecular hydrogen and generally presents the primary kinetic bottleneck in the overall process.[1] Recently, mesoporous cobalt oxide films have received a great deal of attention for their use as catalysts for water oxidation as they operate with high efficiency and relatively low overpotentials in buffered solutions at neutral pHs.[2]

Previous studies have described water oxidation catalysis and electron hopping charge conduction as involving molecular centers uniformly dispersed throughout a homogeneous mesoporous material, taking into account their possible coupling with proton transfer.[3−5] Modeling of catalysis and charge conduction in these systems[4] has accordingly been based on the application of previous analyses[6] to such hypothetic mesoporous molecular structures (Scheme 1 of ref 4). These representations may be considered as working descriptions in the sense that models based on this picture reproduce most of the observable characteristics of the catalytic process and charge conduction in this system. SEM[7] and AFM[8] imaging as well as X-ray PDF[9,10] have indicated that a more accurate structural description is that these films are rather agglomerations of nanoparticles, each made up of coherently stacked cobaltate crystallites and interspersed with phosphate. This is shown schematically in Figure 1. Provided the film is sufficiently thin such that charge percolation between the nanoparticles is not a rate limiting factor, the system should be governed by the mechanism and kinetics of the catalytic process and its association with charge conduction within the nanoparticles.

Starting from this more accurate structural picture, cyclic voltammetry was employed to investigate the mechanistic and kinetic properties of these catalytic films. Full analysis of the effect of scan rate, phosphate concentration and film thickness allowed for the determination of a semiconductor-like charge conduction through the film as well as the identification of discrete molecular-like redox couples at 0.94 and 1.19 V vs SHE. Notably, neither of these couples is associated with the strong catalytic current indicating catalysis occurs from a

Received: January 29, 2016
Published: March 16, 2016

DOI: 10.1021/jacs.6b00737
J. Am. Chem. Soc. 2016, 138, 5615−5622

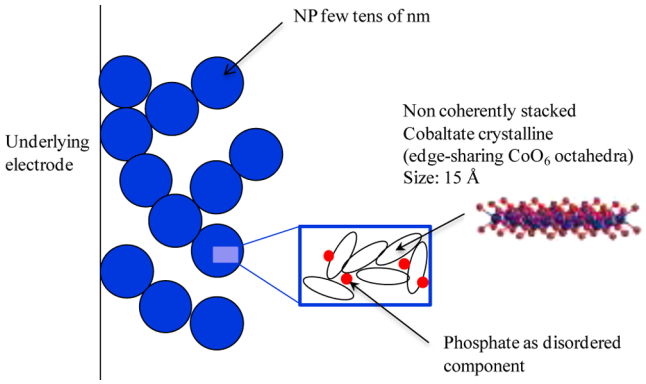

Figure 1. Structural sketch of CoP_i films.

further oxidized species. Analysis of the catalytic current emphasized the role of phosphate as catalyst cofactor and provided low limits for the catalyst standard potential and the rate constant of the reaction.

The results of this study serve to illustrate the molecular-semiconductor duality of phosphate-Co oxides for their applications toward water oxidation catalysis. This is the first identification and characterization of such a heterogeneous-molecular catalyst, which is likely a common motif in other systems.

RESULTS AND DISCUSSION

1. Cyclic Voltammetry of the Catalytic Film. General Features. As detailed in the Experimental Section, the catalytic films were deposited onto a 1 mm diameter *Pt* electrode disk via controlled-potential electrolysis of 0.1 M potassium phosphate (KP_i), pH 7.0, electrolyte solutions containing 0.5 mM Co^{2+}. The charge passed during electrolysis, Ch_{dep}, provides the amount of cobalt deposited onto the electrode surface, $[Co]_{tot}$ assuming a one electron per cobalt transfer:

$$[Co]_{tot}(mol/cm^2) = 1.04 \times 10^{-8} \times Ch_{dep}(mC/cm^2)$$

The thickness of the film was previously estimated from the amount of mol Co/cm^2 determined from ICP analysis of solutions resulting from digestion of the film in 2% nitric acid and from estimation of the volume occupied by each cobalt atom (each Co occupies a cube 5 Å in width),[11,4] the relationship between the thickness, d_f, and the deposition charge per electrode surface area unit, Ch_{dep}:

$$d_f(nm) = 7.8 \times Ch_{dep}(mC/cm^2)$$

These characteristics, summarized in Table 1, allows one to prepare films with desired thicknesses by carefully controlling the amount of charge passed during deposition, Ch_{dep}. Most of our experiments were carried out for thin films so as to avoid charge transfer percolation between the nanoparticles to be rate-limiting. This allowed us to focus attention on our main thrust, namely the mechanism of the catalytic process and of electronic conduction within the nanoparticles.

Table 1. Thin Film Characteristics

Ch_{dep} (mC/cm^2)	$[Co]_{tot}$ (mol/cm^2)	d_f (nm)	C_d (μF)
5	0.52×10^{-7}	39	12
10	1.0×10^{-7}	78	21
20	2.1×10^{-7}	156	38

Figure 2 gives a typical example of cyclic voltammetric current (i)−potential (E) responses of such a thin film and their variations with the scan rate (v). The CV current responses shown as i, $i/\sqrt{v}$ and i/v give a first qualitative picture of the nature of the controlling processes in the various sections of the potential excursion ($i \propto v^0$, $v^{1/2}$, v indicate kinetic control by catalytic reaction, diffusion and surface redox couple or double layer charging capacitive current responses, respectively[12]). Starting around 1.3 V vs SHE, the potential was first scanned cathodically then reversed around 0.6 V vs SHE and further scanned anodically so as to encompass the large catalytic wave before returning to the starting potential. In all cases, CVs were initiated from potentials ≥1.05 V vs SHE as prolonged polarization at lower potentials resulted in film dissolution. The decisive advantage of a transient method such as CV over steady-state methods such as rotating disk electrode

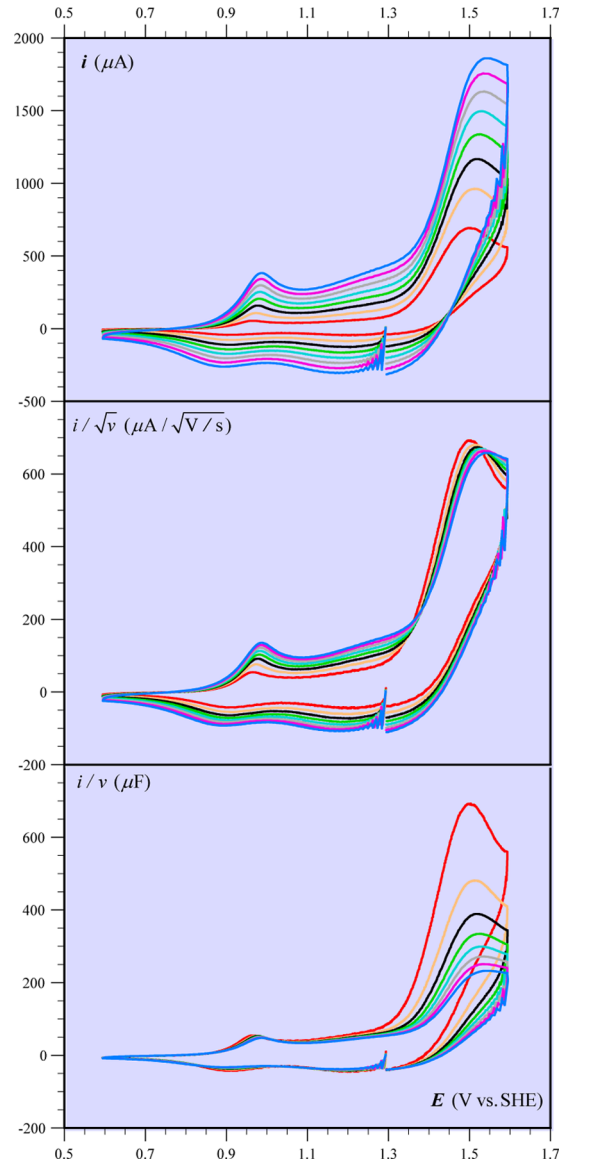

Figure 2. Cyclic voltammetry current (i)−potential responses (E: 1.29 → 0.59 → 1.59 → 1.29 V vs SHE) at various scan rates (v) of a 39 nm CoP_i film in the presence of 0.2 M potassium phosphate, pH = 7. v (V/s): 1 (red), 2 (orange), 3 (black), 4 (green), 5 (cyan), 6 (gray), 7 (magenta), 8 (blue).

DOI: 10.1021/jacs.6b00737
J. Am. Chem. Soc. 2016, 138, 5615−5622

voltammetry (RDEV) clearly appears in the fact that it allows for the detection of surface waves and capacitive responses and is able to discriminate between solution-diffusion control and catalytic kinetic control. We now explore the various potential domains so as to identify the current-governing processes in each of these domains, and, from there, to derive the characteristics of catalysis and conduction.

2. The Conduction and Double Layer Charging Domain. The CV responses obtained in the 1.29 → 0.59 → 1.29 V vs SHE potential domain at low buffer concentration (1 mM potassium phosphate) (Figure 3) are typical of capacitive currents that are proportional of the scan rate.

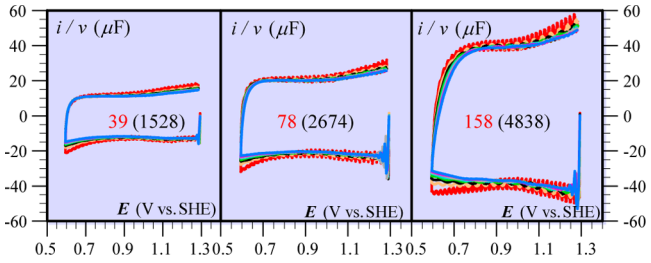

Figure 3. Cyclic voltammetry current (i/v)−potential responses (E: 1.29 → 0.59 → 1.29 V vs SHE) at various scan rates (v) of CoP_i films (pH 7) in the presence of 1 mM P_i and 100 mM KNO_3. v (V/s): 1 (red), 2 (orange), 3 (black), 4 (green), 5 (cyan), 6 (gray), 7 (magenta), 8 (blue). The numbers on each diagram are the values of the film thickness in nm and, between parentheses, the value of the plateau capacitance in $\mu F/cm^2$.

We may infer from these observations that these films behave like electronic conductors in this potential range and that the capacitances are those of the electrical double layer charging. The magnitude of these capacitances is much larger than that of the underlying electrode (typically 20 $\mu F/cm^2$;[13] ~0.2 μF for 1 mm diameter electrode). This is due to the large surface area-solution interface arising from the mesoporous structure of the film as previously discussed (Figure 1).

The capacitance per surface area unit, C_d, increases proportionally with the film thickness: C_d ($\mu F/cm^2$) = 0.25 × d_f (nm) = 1.96 × Ch_{dep} (mC/cm^2) = 1.9 × 10^8 × $[Co]_{tot}$ (mol/cm^2). The surface area of the interface between the solid film and the solution in the pores may then be obtained assuming that the double layer capacitance is related to unit surface area is the same as that of an ideally polarized electrode, i.e., 20 $\mu F/cm^2$.[13] This leads to a surface area of 2 cm^2 for 1 nm-thick film on a 1 cm^2 electrode. (0.2 m^2 for 1 μm-thick film deposited on a 1 cm^2 electrode).

3. Pushing the Potential toward Smaller Values: Passage from a Conductive to an Insulating Film. Starting from the same initial potential but reversing the sweep at progressively lower potentials shows diminished current responses below 0.5 V vs SHE (2 V/s, 1 mM phosphate buffer, 0.1 M KNO_3) (Figure 4). This process is reversible and appears to occur concurrently with a surface-like molecular redox couple response (vide infra).

These observations point to a transition from conducting behavior to insulating behavior. For confirmation, $[Ru^{II}(bpy)_3^{2+}]$ 2$[Cl^-]$ and 1,1′ferrocene di-1-ethanol (E^0 = 1.245 and 0.445 V vs SHE, respectively) were employed as redox probes since the $Ru^{III/II}(bpy)_3^{3+/2+}$ couple lies in the potential range where the film is thought to be conductive

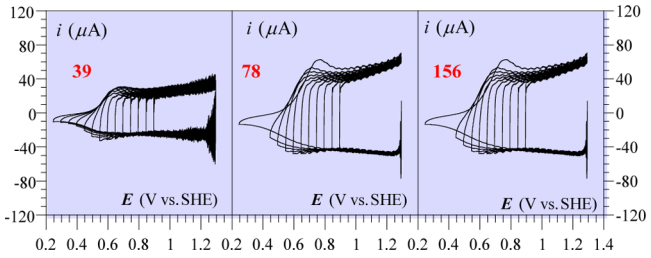

Figure 4. Cyclic voltammetry current (i)−potential responses (E: 1.29 → 0.24 → 1.29 V vs SHE) at 2 V/s of CoP_i films (pH 7) in the presence of 1 mM P_i and 100 mM KNO_3. The numbers on each diagram are the values of the film thickness in nm.

while the 1,1′ferrocene di-1-ethanol couple occurs at potentials where the film is thought to be insulating.

As expected, cyclic voltammograms collected with a ca. 80 nm CoP_i film in the presence of both redox probes indicate the $Ru^{III/II}(bpy)_3^{3+/2+}$ wave is not affected by the presence of the film while the 1,1′ferrocene di-1-ethanol is shifted by roughly 400 mV and appears only when the potential reaches the conductive region. The 1,1′ferrocene di-1-ethanol wave is irreversible since the potential at which re-reduction should occur stands in the potential range where the film is insulating. These observations confirm the conductive/insulating nature of the film and a transition potential that occurs at ~0.5 V vs SHE under these conditions.

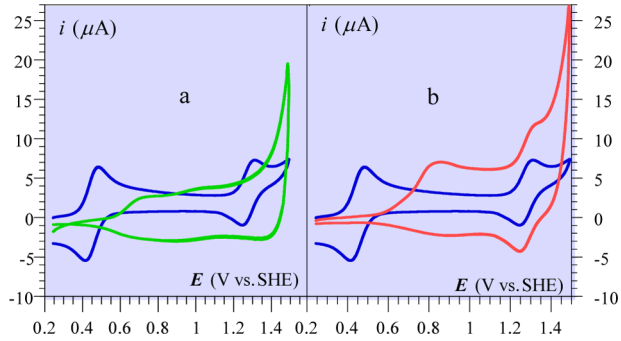

Figure 5. 0.1 V/s CV responses in the presence of 1 mM P_i and 100 mM KNO_3 (pH 7). (a) in blue: 5 ± 1 mM 1,1′-ferrocene-di-1-ethanol (left) and 5 ± 1 mM $[Ru^{II}(bpy)_3^{2+}]2[Cl^-]$ on a bare platinum electrode; in green: 78 nm CoP_i film in the absence of redox probes. (b) in blue: same as in (a); in red: same redox probes in the presence of a 80 nm CoP_i film.

The behavior of CoP_i films in this range of potentials is similar to other mesoporous cobalt oxide materials in that they display p-type semiconductor properties.[14] Much like CoP_i, these and other related systems consist of mesoporous networks of semiconductor crystallites in the nanometer range, permeated by the electrolyte.[15] Due to the structural and electronic similarities, we can conclude the electrochemical behaviors observed with CoP_i are governed by the same principles as those of related mesoporous semiconductors.

P-type semiconductors show insulating behavior when the Fermi level is in the energy gap between the valence and conduction band. When potential is applied, electrons flow from the valence band and associated trapped states to the electrode and the Fermi level lowers. When the Fermi level approaches the valence band edge, the nanostructured film adopts a conducting behavior.

DOI: 10.1021/jacs.6b00737
J. Am. Chem. Soc. 2016, 138, 5615−5622

On the basis of cobalt K-edge X-ray absorption spectroscopy data, in the range of potentials corresponding to this conductive behavior the average cobalt oxidation state is around 3.[16] This means that the valence band consists of overlapping sub-bands originating from 2p O and 3d Co orbitals. Upon anodic polarization, electrons in the valence band are transferred to the electrode and the Fermi level approaches the band edge making the film conductive. Applying a cathodic potential refills these sub-bands and results in the film becoming insulating.

The conductive-to insulating transition is observed around 0.85 V vs SHE in a pH 7 fully buffered solution (≥100 mM P_i, see Figure 7) whereas it occurs at roughly 0.5 V vs SHE in the presence of only 1 mM P_i (Figures 3−5). This is because the transition is pH dependent (i.e., presumably because electron removal is associated with proton removal for charge compensation) and under low buffer conditions the local pH is subject to change due to the proton-coupled nature of the concurrently observed surface wave (vide infra) and the inability of the buffer at low concentrations to successfully mediate this change in proton activity.

4. Assignment of the Redox Couples in the Film and of the Catalytic Current−Potential Response. As seen in Figure 4, peaks appear on top of the flat capacitive current, more clearly on the anodic scan than on the cathodic scan. They become more apparent when the concentration of P_i is increased. Subtraction of the capacitive component of the current, i_C, both on the cathodic and anodic scan (Figure 6) allows a better characterization of these faradaic responses and of their variations with $[P_i]$. The values of the capacitive component are obtained from the capacitances, C_d, derived ($i_C = S{\cdot}C_d{\cdot}\nu$, S being the geometric surface) from the experiments shown in Figure 3 (C_d values in parentheses). As noted earlier, the potential of the insulator-conductive behavior transition is sensitive to buffer concentration, presumably due to changes in local pH associated with the proton-coupled nature of this redox process. Therefore, quantification of the faradaic current obtained by current subtraction of the capacitive component contains a non-negligible amount of uncertainty in the 0.6−0.9 V vs SHE region. Three faradaic responses, which increase with the concentration of buffer, can be detected: two reversible processes (indicated by the vertical arrows in Figure 6) corresponding to apparent standard potentials at 0.94 and 1.19 V vs SHE and a catalytic process at more positive potential (indicated by the horizontal arrows in Figure 6). The reversible processes are scan rate dependent but less than proportional to ν, thus indicating interference of diffusion, in line with the strong dependence of these responses on $[P_i]$.

The reversible processes may be assigned to cobalt redox species involving Co^{III}/Co^{II} and Co^{IV}/Co^{III} couples, respectively. Similar couples have been previously reported based on spectro-electrochemical measurements although in this case the $Co^{IV/III}$ response was thought to be related to the catalysis.[16]

It is clearly apparent in Figure 6, the Co^{IV}/Co^{III} couple is not responsible for the large catalytic response, although it may show very slow catalysis as noted in ref 5.[17] Taking these observations into account, our data indicate that the main catalytic reaction, which actually makes these CoP_i films good water oxidation catalysts, requires the formation of a further oxidized Co species.

On the basis of the observation that the Co^{III}/Co^{II} and Co^{IV}/Co^{III} waves are both sensitive to pH and to the nature of the buffer,[7b] both redox processes may be viewed as proton-coupled-electron transfer (PCET) reactions and may thus be globally written as

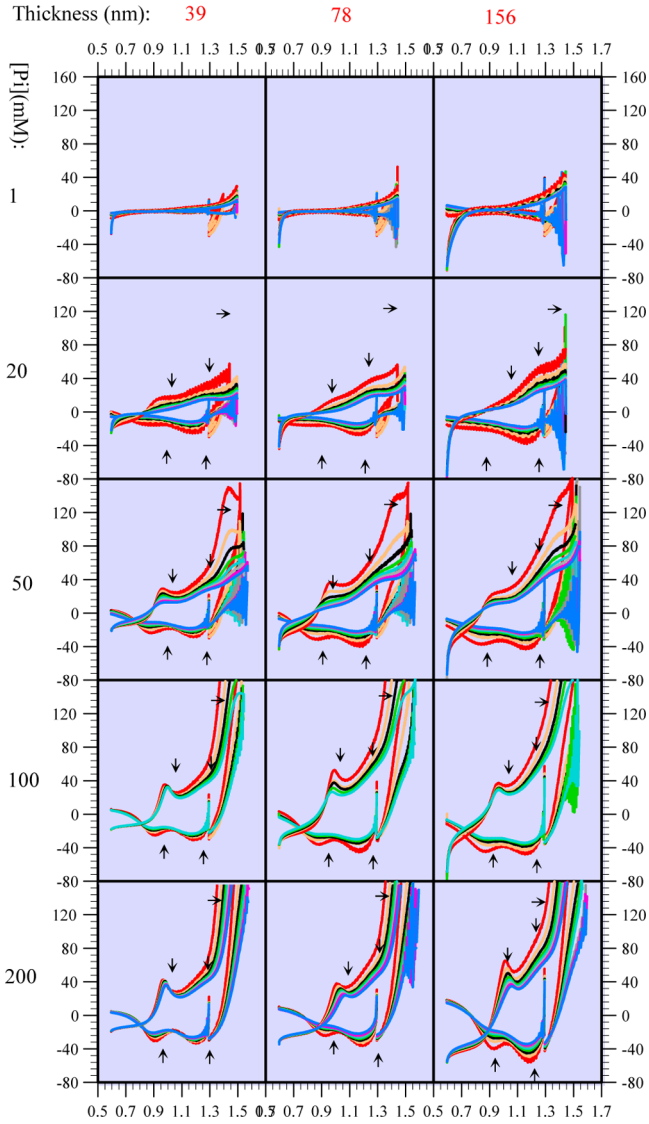

Figure 6. CV scan rate normalized current (ordinate in $\mu A/V\ s^{-1}$) potential (abscissa in V vs SHE) responses of CoP_i films (pH 7) after subtraction of a constant capacitive current i_C (see text) as a function of the film thickness (numbers on top of the figure), of $[P_i]$ (numbers on the left of the figure) and the scan rate ν (in V/s): 1 (blue), 2 (red), 3 (green), 4 (magenta), 5 (yellow), 6 (dark yellow), 7 (navy), 8 (purple). Each scan is started cathodically at 1.29 V vs SHE. The black vertical arrows indicate the faradaic redox processes and the horizontal arrows the catalytic current (see text).

$$Co^{II}OH_2 + B^- \rightleftharpoons e^- + Co^{III}OH + BH \quad \text{(i)}$$

$$Co^{III}OH + B^- \rightleftharpoons e^- + Co^{IV}O + BH \quad \text{(ii)}$$

where the Co species are adsorbed and B^- and BH are freely diffusing buffer components.

5. Quantitative Analysis of the Co^{III}/Co^{II} and Co^{IV}/Co^{III} Current−Potential Responses. Reaction i and ii involve both adsorbed reactants—the cobalt redox couples—and freely diffusing co-reactants in solution—the buffer components. The current−potential responses may thus pass from a surface wave behavior to a solution diffusion-controlled behavior[12] upon varying operational parameters such as scan rate (ν), buffer

DOI: 10.1021/jacs.6b00737
J. Am. Chem. Soc. 2016, 138, 5615−5622

concentration (C_b = [B-bulk] + [BH-bulk]) and surface concentration of redox reactants deposited on the electrode surface (Γ^0). It can be shown (see Supporting Information (SI)) that, in the framework of the above PCET processes, the dimensionless peak current,

$$\psi_p = \frac{i_p}{FSC_b\sqrt{D}\sqrt{\frac{Fv}{RT}}} \quad (1)$$

is a function of the dimensionless parameter p representing the competition between the two behaviors:

$$p = \frac{\Gamma^0}{C_b\sqrt{\frac{DRT}{Fv}}} \quad (2)$$

where i_p is the cathodic peak current and D, the diffusion coefficient of the two buffer components.

At low scan rates, high buffer concentrations and small values of Γ^0 (thin films), a surface wave is expected. This is shown by the black curve in Figure 7a which models a Nernstian PCET surface reaction with freely diffusing buffer in solution. The experimental data (Figure 7b, blue trace) display peak widths

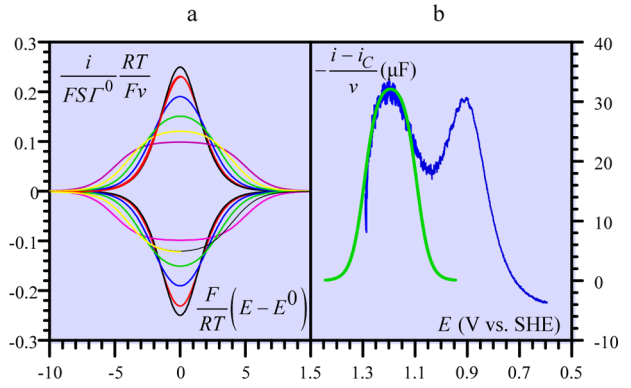

Figure 7. (a) Dimensionless current–potential responses of the surface wave type (p = 0) as a function of the dimensionless standard potential distribution parameter: $F\Delta E^0/RT$ = 0 (black), 1 (red), 2 (blue), 3 (green), 4 (yellow), 5 (magenta). (b) Blue: experimental current–potential cathodic response for a 39 nm film ($[Co]_{tot}$ = 0.52 × 10^{-7} mol/cm^2) after subtraction of the capacitive current in the presence of 200 mM of P_i ([B-bulk] = [BH bulk]) at 0.1 V/s. Cathodic scan starting at 1.29 V vs SHE. Green: fit with the $F\Delta E^0/RT$ = 4 working curve of (a) and Γ^0 = 8 × 10^{-9} mol/cm^2.

broader than what is predicted by this model, suggesting a distribution of potentials centered the apparent standard potential E^0.[18] For the sake of simplicity, we consider a rectangle distribution of ΔE^0 width (see SI) rather than a Gaussian distribution of standard potentials.[18] This leads to the introduction a dimensionless standard potential distribution parameter: $F\Delta E^0/RT$. Figure 7a shows how the normalized CV surface waves vary with this parameter. Using the value $F\Delta E^0/RT$ = 4, determined from fitting optimization, (Figure 7b, green trace figure) we may now analyze the experimental response for reaction 2 shown in Figure 7b. Analysis of reaction ii is simpler than for reaction i where the contribution of wave tailing at lower potentials introduces fitting complications.

Γ^0 is proportional to the film thickness and to the total number of moles of Co deposited. Introducing, e.g., γ as the proportionality factor between Γ^0 and $[Co]_{tot}$: $\Gamma^0 = \gamma\,[Co]_{tot}$. p may thus be expressed as

$$p = \frac{\gamma[Co]_{tot}}{C_b\sqrt{DRT/Fv}} \quad (3)$$

All experimental values of the cathodic peak current of the Co^{III}/ Co^{IV} wave may thus be plotted as a function of log p, selecting a value of γ such that all data points fall on to the same ψ_p – log p theoretical curve. This is shown in Figure 8 with γ = 0.086.

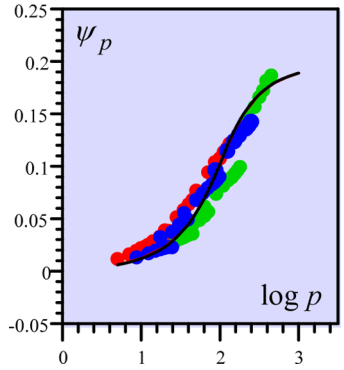

Figure 8. Dimensionless cathodic peak current (eq 1) potential of the same three CoP_i thin films as in Figure 6 of thickness (nm): 39 (red dots); 78 (blue dots), 156 (green dots) for $[P_i]$ = 20, 50, 100, 200 mM and scan rates: 1, 2, 3, 4, 5, 6, 7, 8 V/s, γ in eq 3 being taken as equal to 0.086 so as to make all data points fit with a single theoretical (black) line.

It follows that the Co^{IV}/Co^{III} and Co^{III}/Co^{II} couples are only a very small fraction, ca. 9%, of the total amount of cobalt present in the films.

6. Quantitative Analysis of the Catalytic Current–Potential Response. It results from the discussion in section 3 that the catalytic reaction requires further electron transfer beyond Co^{IV}. From the observation that the CV responses depend of the pK_a of the buffer (Figure 9), it is apparent this

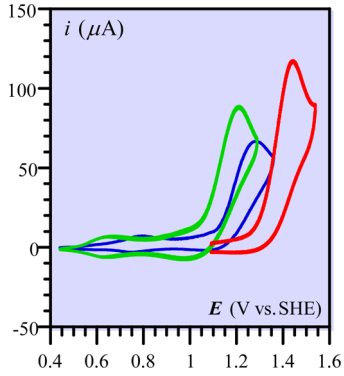

Figure 9. CV responses of 39 nm films obtained from various buffer (phosphate: red, borate: blue; carbonate: green) and run at 0.1 V/s in the corresponding 0.1 M buffer solution at pH 7 (phosphate), 9.2 (borate), 10.3 (carbonate).

redox process involves the coupled transfer of a proton. On the basis of previous descriptions,[2,19] we refer to this process formally as a $Co^{III}Co^{IV}/Co^{IV}Co^{IV}$ proton coupled redox couple occurring from molecular-like cobalt dimers in the film (presumably at the edge of the cobaltate clusters) leading to the reaction scheme shown on Scheme 1.[20]

DOI: 10.1021/jacs.6b00737
J. Am. Chem. Soc. 2016, 138, 5615–5622

Scheme 1

$$HOCo^{III}Co^{IV}O + B^- \overset{E^\circ_{cat}}{\rightleftharpoons} OCo^{IV}Co^{IV}O + BH + e^-$$

$$OCo^{IV}Co^{IV}O + 2\,H_2O \xrightarrow{k_{cat}} H_2OCo^{II}Co^{II}OH_2 + O_2$$

$$H_2OCo^{II}Co^{II}OH_2 + B^- \overset{E^\circ<E^\circ_{cat}}{\rightleftharpoons} e^- + HOCo^{III}Co^{II}OH_2 + BH$$

$$HOCo^{III}Co^{II}OH_2 + B^- \overset{E^\circ<E^\circ_{cat}}{\rightleftharpoons} e^- + HOCo^{III}Co^{III}OH + BH$$

$$HOCo^{III}Co^{III}OH + B^- \overset{E^\circ<E^\circ_{cat}}{\rightleftharpoons} e^- + HOCo^{III}Co^{IV}O + BH$$

$$2\,H_2O + 4\,B^- \longrightarrow O_2 + 4\,BH + 4\,e^-$$

We restrict the analysis of the catalytic CV responses to our thinnest films (a 39 nm film deposited on a 1 mm diameter platinum electrode) in order to minimize the effect of charge transport through the film and therefore maximize the kinetic control by the catalytic reaction, whose characterization is our main thrust. The variation of these responses with phosphate concentration and scan rate are summarized in Figure 10.

The fact that peaks are observed and the peak current is proportional to $[Pi] \times \sqrt{v}$ (Figure 10, bottom left) is an indication that pure kinetic conditions are achieved and a total catalysis regime is established.[12] Kinetic analyses of such processes have been worked out in the absence of catalyst cofactor but are not applicable here. These analyses and the ensuing relationships relating the CV responses to the characteristic parameters of the system have been adapted to the present case where the catalyst (CoP_i) stands on the electrode surface and the catalyst cofactor (P_i) and substrate (H_2O) are homogeneously dispersed in solution. Taking additionally into account the standard potential distribution introduced earlier, the peak characteristics given by the following equations (see SI):

$$i_p = 0.24FS[Pi]\sqrt{\frac{DFv}{RT}} \tag{4}$$

$$E_p = E^0_{cat} + 0.65\frac{RT}{F} + \frac{RT\ln 10}{F}\log\left(\frac{[Pi]\sqrt{\frac{DFv}{RT}}}{\Gamma^0 4k_{cat}}\right) + \frac{RT\ln 10}{F}\log\left(\frac{F\Delta E^0/RT}{\sinh(F\Delta E^0/RT)}\right) \tag{5}$$

For small values of $[Pi] \times \sqrt{v}$, the peak potential is predicted to vary as follows: $\frac{\partial E_p}{\log([Pi]\times\sqrt{v})} = \frac{RT}{F\ln 10}$. Application of eq 5 then leads to[21]

$$E^0_{cat} - \frac{RT}{F\ln 10}\log 4k_{cat} = 1.36\text{V vs SHE} \tag{6}$$

where $F\Delta E^0/RT = 4$, $\Gamma^0 = 4.5 \times 10^{-9}$ mol/cm^2 and $D = 8 \times 10^{-6}$ cm^2/s.[22]

CVs collected using very thin films and sufficiently high scan rates/buffer concentrations should result in a scenario where buffer diffusion no longer plays a role in the current response. In this case a plateau-shaped voltammogram would be expected with a plateau current related to the kinetic rate constant, k_{cat}, by eq 7.

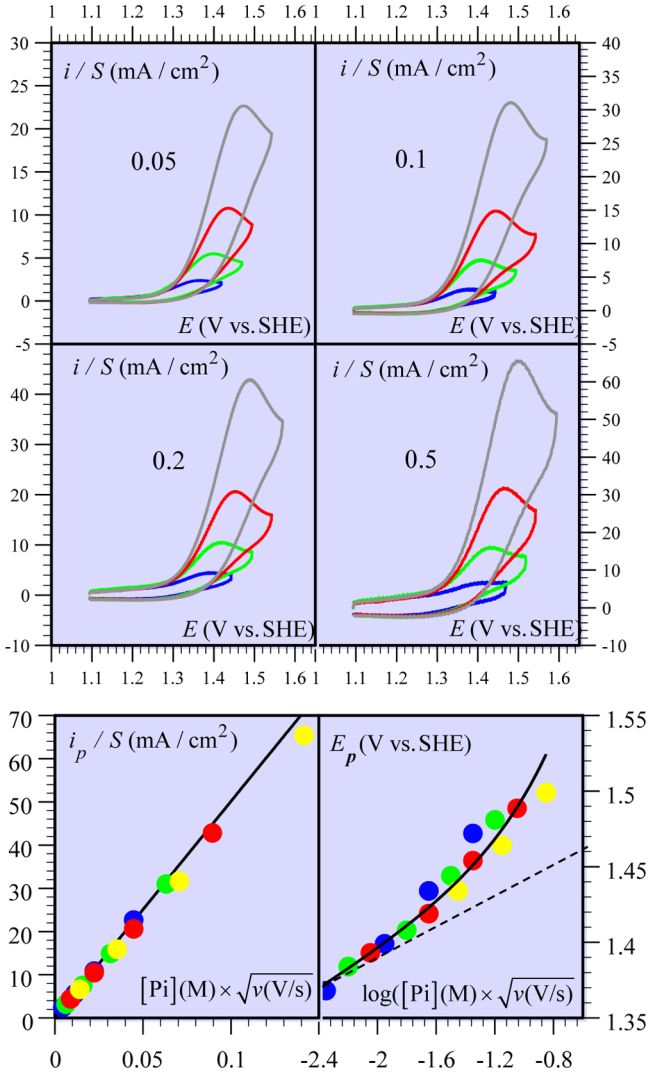

Figure 10. CV responses of a 39 nm film obtained at various scan rates (numbers in the four upper diagrams in V/s) for increasing concentrations of phosphate (in M): 0.02 (blue), 0.05 (green), 0.1 (red), 0.2 (gray). Bottom left: variation of the peak current density with the $[Pi] \times \sqrt{v}$ product, in line with the predictions of eq 4. Bottom right: variation of the peak potential with the $[Pi] \times \sqrt{v}$ product (see text), dashed line: predictions of eq 4.

$$\frac{i_{max}}{FS} = 4\Gamma^0 k_{cat} \tag{7}$$

Reaching this type of limiting behavior is desirable since it allows E^0_{cat} and k_{cat} to be determined separately. In our case, we were unable to reach such limiting behavior even with very thin films, fast scan rates and high buffer concentrations. None the less, since the buffer diffusion-limited peak current observed for a given set of CV parameters is *smaller* than the plateau current that would be observed in the absence of buffer diffusion interference, the peak current measured for our thinnest film (39 nm; $\Gamma^0 = 4.5 \times 10^{-9}$ mol cm^{-2}), highest buffer concentration (0.2 M) and fastest scan rate (8 V/s) provides a low limit for a non diffusion-limited current response from which a low limit for the catalytic rate constant, k_{cat}, can be determined using eq 7: $k_{cat} \geq 112.5$ s^{-1}.

Inserting this limit for k_{cat} into eq 6 then yields a low limit for the catalyst apparent standard potential:

DOI: 10.1021/jacs.6b00737
J. Am. Chem. Soc. 2016, 138, 5615−5622

$E^0_{cat} \geq 1.51$V vs SHE

Turning our attention to the dependence of the peak potential on $\log([Pi] \times \sqrt{\nu})$, we note a deviation from the behavior expected from eq 5 (Figure 10, bottom right) that cannot be attributed to ohmic drop in the solution. This suggests that, despite its extreme thinness, potential drop resulting from charge transport through the mesoporous film begins to interfere as more current flows through the system. Strictly speaking, charge transport through the mesoporous film cannot be likened to a mere ohmic drop effects in systems involving a metallic electrode immersed in an electrolyte solution. A rigorous approach of the problem, currently under our examination, requires modeling the system along a transmission line scheme[23] accounting for the time-dependence of the potential profiles in the film.

The importance of these effects points to the necessity of improving charge transport in the film to render catalysis more effective. For example, the use of thicker films aiming at larger catalytic currents is severely limited by charge transport.

CONCLUSIONS

A systematic cyclic voltammetric study was carried with electrodeposited CoP_i to provide insights regarding the mode of charge transport and the mechanism of catalytic water oxidation that occurs in the films. Under low $[P_i]$ conditions, variation of the film thickness and scan rate at potentials below the catalytic wave indicate CoP_i is conductive at potentials above the 0.80 V vs SHE (pH = 7) and becomes insulating at lower potentials. We attribute this conductive nature to the mesoporous structure of the film which behaves like a bulk p-type semiconductor. Introducing higher concentrations of P_i buffer and increasing the sweep width to include the catalytic process shows the appearance of two discrete proton-coupled redox couples that appear on top of the large capacitive current and prior to the catalytic wave. These waves are assigned as $Co^{III/II}$ and $Co^{III/IV}$ couples. Careful modeling of these waves indicates they represent only ~10% of the total Co in the film suggesting only a small fraction of the further oxidized Co is responsible for the strong catalysis observed at higher potentials.

Formulation and application of a model for the current−potential response related to the catalytic wave allowed it to be determined that catalysis is mostly limited by diffusion of the P_i buffer and provided high limits for the catalyst apparent standard potential and catalytic rate constant: $E^0_{cat} \geq 1.51$ V vs SHE, $k_{cat} \geq 112.5$ s^{-1}. Although catalysis is *mostly* limited by P_i diffusion, slightly diminished currents are observed as film thickness is increased due to the interference of slow charge transport kinetics in the film. It should be emphasized that all of the films used in this study were very thin relative to what might be used in an actual device. It follows that with thicker, more practically attractive films charge transport kinetics will present an appreciable bottleneck to catalysis. Future efforts toward optimizing the catalytic performance of these materials should therefore be focused on improving the film conductivity.

In addition to providing qualitative and quantitative information regarding water oxidation catalysis with CoP_i, these results clearly demonstrate the coexistence of both bulk semiconductor and molecular qualities in these films. The cooperativity of these properties appears to be critical for the success of the catalyst in that molecular sites are necessary to perform the catalytic reaction but bulk conducting properties are required to ensure efficient charge transport from the electrode through the film. This somewhat surprising conclusion is counterintuitive to the commonly held notion that bulk and molecular species are governed by different fundamental principles but is likely to be a general motif present in other efficient electrocatalytic films.

EXPERIMENTAL SECTION

Materials. All solutions were prepared using Milli-Q water. $Co(NO_3)\cdot 6H_2O$ (99.8%), KOH (≥85%), KNO_3 (≥99%), KH_2PO_4 (≥99%) and $[Ru^{II}(bpy)_3^{2+}]$ $2[Cl^-]$ were purchased from Sigma and used as received. 1,1′-Ferrocene di-1-ethanol was prepared as previously described.[24] The Pt electrode (1 mm diameter) was purchased from Metrohm. Electrodes were polished with alumina paste on microcloth pads prior to use. The electrode surfaces were cleaned by electrochemical cycling in ~0.2 M HNO_3 (sweeps between 0.24 and −0.31 V vs SHE, 1 V/s, ×10) then anodized at 1.44 V vs SHE for ~5 min prior to film deposition.

Electrochemical Methods. Cyclic voltammetric measurements were carried out using an Autolab potentiostat (PGSTAT12), an SCE reference electrode (Radiometer Analytical), and a Pt wire counter electrode. Electrode potentials were converted to SHE from SCE using $E(SHE) = E(SCE) + 0.24$ V. All experiments were carried out at ambient temperatures (23 ± 1 °C) in 50 mL beakers. Between experiments, the cell was kept at a constant resting potential of 1.09 V vs SHE to prevent slow film degradation that occurs at open circuit potential. Unless otherwise stated, all solutions were adjusted to pH 7 and contained 0.1 M KNO_3 in addition to phosphate buffer, P_i.

Film Preparation. Catalyst films were prepared as previously described.[4] Prior to data collection, films were subjected to repeated cyclic voltammetric scans in a pH 7, 0.1 M P_i solution sweeping through the catalytic wave (1.09 to 1.44 V vs SHE, 100 mV/s) until the voltammograms remained constant between scans (typically 3−5 scans).

Cyclic Voltammetry. CVs were recorded in P_i/KNO_3, pH 7 solutions. In all cases, the cell resting potential immediately prior to scan initiation was 1.09 V vs SHE and positive feedback compensation was used to minimize the ohmic drop between the working and reference electrodes. For each film thickness and P_i solution, three separate films were prepared and used for data collection. In all cases, excellent reproducibility was observed between different films under all conditions reported here.

ASSOCIATED CONTENT

Supporting Information

The Supporting Information is available free of charge on the ACS Publications website at DOI: 10.1021/jacs.6b00737.

Formal analysis of a PCET-catalytic mechanism; effect of potential distribution. (PDF)

AUTHOR INFORMATION

Corresponding Authors

*saveant@univ-paris-diderot.fr

*cyrille.costentin@univ-paris-diderot.fr

Notes

The authors declare no competing financial interest.

ACKNOWLEDGMENTS

Partial support from the Agence Nationale de la Recherche (ANR CATMEC 14-CE05-0014-01) is acknowledged.

REFERENCES

(1) Eisenberg, R.; Gray, H. B. *Inorg. Chem.* **2008**, *47*, 1697.

(2) Bediako, D. K.; Ullman, A. M.; Nocera, D. G. *Top. Curr. Chem.* **2015**, *371*, 173.

DOI: 10.1021/jacs.6b00737
J. Am. Chem. Soc. 2016, 138, 5615−5622

(3) Kanan, M. W.; Surendranath, Y.; Nocera, D. G. *Chem. Soc. Rev.* **2009**, *38*, 109.
(4) Bediako, D. K.; Costentin, C.; Jones, E. C.; Nocera, D. G.; Savéant, J.-M. *J. Am. Chem. Soc.* **2013**, *135*, 10492.
(5) Ahn, H. S.; Bard, A. J. *J. Am. Chem. Soc.* **2015**, *137*, 612.
(6) (a) Andrieux, C. P.; Savéant, J.-M. *Catalysis at Redox Polymer Coated Electrodes. In Molecular Design of Electrode Surfaces*; Murray, R. W., Ed.; John Wiley & Sons: New York, NY, 1992; Vol. *22*, pp 207−270. (b) Savéant, J.-M. *Chem. Rev.* **2008**, *108*, 2348.
(7) (a) Kanan, M.; Nocera, D. G. *Science* **2008**, *321*, 1072. (b) Surendranath, Y.; Dinca, M.; Nocera, D. G. *J. Am. Chem. Soc.* **2009**, *131*, 2615.
(8) Liu, Y.; Nocera, D. G. *J. Phys. Chem. C* **2014**, *118*, 17060.
(9) Du, P.; Kokhan, O.; Chapman, K. W.; Chupas, P. J.; Tiede, D. M. *J. Am. Chem. Soc.* **2012**, *134*, 11096.
(10) Farrow, C. L.; Bediako, D. K.; Surendranath, Y.; Nocera, D. G.; Billinge, S. L. *J. Am. Chem. Soc.* **2013**, *135*, 6403.
(11) (a) Surendranath, Y.; Kanan, M. W.; Nocera, D. G. *J. Am. Chem. Soc.* **2010**, *132*, 16501. (b) In this estimation we assume that the surface area of the electrode occupied by the pores is negligibly small as compared to that occupied by the CoP_i. This assumption is justified by the observation that under its insulating form, the film totally blocks the access to the electrode surface of electroactive molecules as described and discussed in the following.
(12) Savéant, J.-M. *Elements of Molecular and Biomolecular Electrochemistry: An Electrochemical Approach to Electron Transfer Chemistry*; John Wiley & Sons: Hoboken, NJ, 2006.
(13) Pajkossy, T.; Kolb, D. M. *Electrochem. Commun.* **2007**, *9*, 1171.
(14) (a) Schumacher, L. C.; Holzhuetter, I. B.; Hill, I. R.; Dignam, M. J. *Electrochim. Acta* **1990**, *35*, 975. (b) Barreca, D.; Massigna, C.; Daolio, S.; Fabrizio, M.; Piccirillo, C.; Armelao, L.; Tondello, E. *Chem. Mater.* **2001**, *13*, 588.
(15) (a) Fabregat-Santiago, F.; Mora- Seró, I.; Garcia-Belmonte, G.; Bisquert, J. *J. Phys. Chem. B* **2003**, *107*, 758−68. (b) Bisquert, J.; Zaban, A. *Appl. Phys. A: Mater. Sci. Process.* **2003**, *77*, 507. (c) Berger, T.; Molinor-Satoca, D.; Jankulovska, M.; Lana-Villarreal, T.; Gomez, R. *ChemPhysChem* **2012**, *13*, 2824. (d) Bisquert, J.; Fabregat-Santiago, F.; Mora-Sero, I.; Garcia-Belmonte, G.; Barea, E. M.; Palomares, E. *Inorg. Chim. Acta* **2008**, *361*, 684.
(16) Risch, M.; Ringleb, F.; Kohlhoff, M.; Bogdanoff, P.; Chernev, P.; Zaharieva, I.; Dau, H. *Energy Environ. Sci.* **2015**, *8*, 661.
(17) A rate constant of 3.2 s^{-1} was thus reported. In CV, the corresponding value of the dimensionless parameter $\lambda_{cat} = (RT/F)(k_{cat}/v) = 0.1$ is too small to produce a significant catalytic increase of the current as soon as $v > 0.8$ V s^{-1}.
(18) Rowe, G. K.; Carter, M. T.; Richardson, J. N.; Murray, R. W. *Langmuir* **1995**, *11*, 1797.
(19) (a) Zhang, M.; Frei, H. *Catal. Lett.* **2015**, *145*, 420. (b) Zhang, M.; de Respinis, M.; Frei, H. *Nat. Chem.* **2014**, *6*, 362.
(20) (a) Generation of the active form of the catalyst may also be described as formation of a formally Co^V species[20b,c] coupled to the removal of a surrounding proton thus leading to an alternative but equivalent reaction scheme as depicted in Scheme 1. The broad distribution of standard potentials, however, seems to indicate a strong interaction of the active site with neighboring cobalt centers, which would be the case for dimeric forms. (b) Li, X.; Siegbahn, P. E. M. *J. Am. Chem. Soc.* **2013**, *135*, 13804. (c) Nguyen, A. I.; Ziegler, M. S.; Ona-Burgos, P.; Sturzbecher-Hoehne, M.; Kim, W.; Bellone, D. E.; Tilley, T. D. *J. Am. Chem. Soc.* **2015**, *137*, 12865.
(21) It is also worth noting that the present results give practically the same value of $E^0_{cat} - (RT/F \ln 10)\log k_{cat}$ (= 1.26 V vs SHE) as that previously derived from rotating disk electrode data obtained with the same system in a potential range located at the very foot of the catalytic wave, also noting that in this previous no potential distribution was considered, thus neglecting the term $\frac{RT \ln 10}{F} \log\left(\frac{F\Delta E^0/RT}{\sinh(F\Delta E^0/RT)}\right) \approx 0.07\text{V}$.[4]
(22) *Handbook of Chemistry and Physics*, 81st ed.; Lide, D. R., Ed.; CRC Press: Boca Raton, FL, 2000−2001; pp 5−96.
(23) (a) De Levie, R. *Electrochim. Acta* **1963**, *8*, 751. (b) Bisquert, J.; Garcia-Belmonte, G.; Fabregat-Santiago, F.; Compte, A. *Electrochem. Commun.* **1999**, *1*, 429.
(24) Graham, P. J.; Lindsey, R. V.; Parshall, G. W.; Peterson, M. L.; Whitman, G. M. *J. Am. Chem. Soc.* **1957**, *79*, 3416.

DOI: 10.1021/jacs.6b00737
J. Am. Chem. Soc. 2016, 138, 5615−5622